Science of the Total Environment 865 (2023) 161072

Contents lists available at ScienceDirect

Science of the Total Environment

journal homepage: www.elsevier.com/locate/scitotenv

Does flooding get worse with subsiding land? Investigating the impacts of land subsidence on flood inundation from Hurricane Harvey

Han Jiang [a,1], Jiaqi Zhang [b,1], Yi Liu [c], Jiang Li [c], Zheng N. Fang [a,*]

[a] Department of Civil Engineering, University of Texas at Arlington, Arlington, TX, USA
[b] School of Civil Engineering and Environmental Science, University of Oklahoma, Norman, OK, USA
[c] Department of Civil Engineering, Morgan State University, Baltimore, MD, USA

HIGHLIGHTS

- Retrospective land subsidence of 117 years is investigated with respect to the impact on flood inundation.
- Hydrodynamic simulation reveals the impacts from land subsidence regarding flood depth, inundation extent, and flow velocity.
- The effects of land subsidence on flooding are not only heterogeneous but even mixed with both positive and negative impacts.

GRAPHICAL ABSTRACT

Schematic flowchart of flood inundation modeling with land subsidence information. First, one hundred and seventeen years of land subsidence is simulated by a physics-based modeling considering groundwater withdrawal and the consequent aquifer-system compaction. Then flood inundation mapping from Hurricane Harvey is conducted by a hydrodynamic model over the topologies in different historical times from 1900 to 2017 to investigate the impacts from land subsidence.

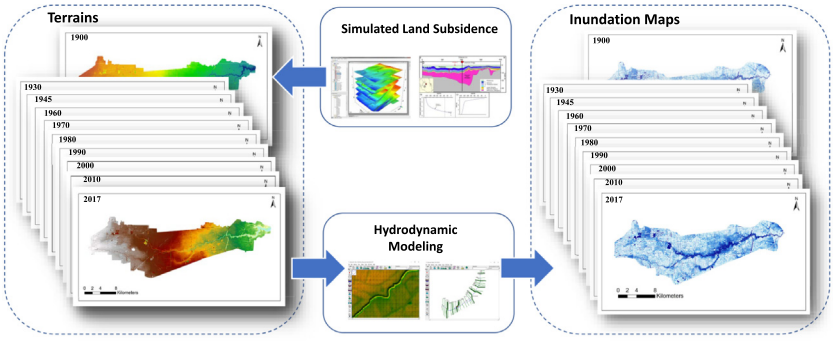

ARTICLE INFO

Editor: Fernando A.L. Pacheco

Keywords:
Land subsidence
Hurricane Harvey
Flood inundation
Flood extent
Flood depth and velocity
HEC-RAS 2D modeling

ABSTRACT

As one of the most devastating tropical storms, 2017 Hurricane Harvey caused severe flooding and damage in Houston, Texas. Besides enormous rainfall amount, land subsidence might be another contributing factor to the Harvey flood. However, few studies have numerically quantified the evolvement of land subsidence over decades, largely due to the lack of reliable methods to realistically estimate land subsidence both continuously and at high spatial resolution. Therefore, this study aims to investigate retrospective changes of regional topology due to 117 years (1900 to 2017) of land subsidence and the consequent impacts on flood inundation. Based on continuous land subsidence, we conduct a series of simulations on the 2017 Hurricane Harvey in Brays Bayou, Texas using a hydrodynamic/hydraulic model. The results indicate that the overall change of flood depth caused by land subsidence is relatively minor with the flood water deepened by six centimeters per one meter of subsided land at the worst impacted location. The impact from land subsidence on flood depth exhibits strong nonlinearity in time, where effects from previous land subsidence hotspots could be altered by later continuing land subsidence. Spatially, changes in flood depth due to the land subsidence are not only heterogeneous but mixed with coexisting increased and reduced flood depths. The results of this study improve the understanding of the dynamic evolvement of flood inundation due to continuous land subsidence so that better planning can be initiated for sustainable urban development for coastal communities, which is imperative under ongoing climate change and sea level rise.

* Corresponding author.
E-mail address: nickfang@uta.edu (Z.N. Fang).
[1] Shared Co-first authorship. These authors contributed equally to this work.

http://dx.doi.org/10.1016/j.scitotenv.2022.161072
Received 21 August 2022; Received in revised form 6 December 2022; Accepted 16 December 2022
Available online 27 December 2022

1. Introduction

Flood is one of the most destructive natural disasters throughout the world (Kellens et al., 2013; Munawar et al., 2019; Ahmadlou et al., 2021; Shareef and Abdulrazzaq, 2021). Not only does it pose a great threat to human beings and their living environment, but it also causes severe damage to the economy (Penning-Rowsell et al., 2005; Khan et al., 2010; Michel-Kerjan and Kunreuther, 2011; Patel et al., 2017; Farooq et al., 2019; Kim et al., 2020). Based on the international disaster database, flooding has resulted in a total loss of over $870 billion globally since 1900 (EM-DAT, 2020). In the United States (U.S.) alone, flooding has caused more than $68 billion in loss between 1970 and 2019 (FEMA, 2020). As one of the most devastating events, 2017 Hurricane Harvey produced the largest rainfall of any U.S. hurricane on record (Emanuel, 2017) with the maximum four-day rainfall exceeding 1000-year return period in most of Houston-Beaumont region (HDSC, 2017). During the severe flooding caused by Hurricane Harvey, numerous houses damaged are located even outside of the 500-year floodplain areas (Jonkman et al., 2018; Miller and Shirzaei, 2019). The unprecedent nature of the Harvey floods calls for a significant advancement in understanding of the processes of determining flood risk and severity.

Besides climate variability and changes, several studies have shown that anthropogenic and natural changes to the land surface (e.g., land subsidence) might exacerbate flooding issues (e.g., Rodolfo and Siringan, 2006; Hanson et al., 2011; Viero et al., 2019; Ouyang et al., 2020). Especially for the flat-lying coastal areas, land subsidence would increase the potential for flooding caused by tides and storm surges (Holzer and Johnson, 1985). Dixon et al. (2006) found the failure of the levees during Hurricane Katrina could be caused by land subsidence in New Orleans. A study done by Wang et al. (2012) indicated land subsidence affects coastal seawalls and flood-control levees in Shanghai, leading to changes in floodplain boundaries. Moreover, Ouyang et al. (2020) analyzed the local land subsidence caused by 2011 Tohoku earthquake in Japan and found the inundation areas would be underestimated by around 10 % if only considering rainfalls without considering the effect of land subsidence. In the U.S., land subsidence happens in many urbanized areas with over 44,000 km^2 across 45 states, and among all the affected areas, the Houston-Galveston area experienced land subsidence as early as 1900s (Stork and Sneed, 2002). The main causes of land subsidence in this area are the exploitation of groundwater, extraction of oil and gas, and depletion of hydrocarbon reservoirs (Holzer and Bluntzer, 1984; Galloway et al., 1999). Based on a report conducted by the United States Geological Survey (USGS), land subsidence in Houston-Galveston region continued throughout the 20th century (Stork and Sneed, 2002). Even until recent years, land subsidence of >10 mm/year and up to 25 mm/year is still happening in inland areas north and west of the City of Houston (Yu et al., 2014). Hence, it is important to evaluate flood impacts in regions prone to land subsidence.

To investigate the impacts of land subsidence on inundation, remote sensing observation has been utilized by previous studies. For instance, Shirzaei and Bürgmann (2018) utilized interferometric synthetic aperture radar (InSAR) and global navigation satellite system to estimate the land subsidence rate in the San Francisco Bay Area and generated the future 100-year inundation maps based on probabilistic projections of sea level rise. Similarly, Catalao et al. (2020) also used InSAR measurements to estimate land subsidence and combined with future sea level rise scenarios to identify the projected flood inundation areas in Singapore. Other than these projection/scenario-based studies, Miller and Shirzaei (2019) analyzed the flood inundation extent of Hurricane Harvey derived from satellite images and correlated it with land subsidence data in two different historical periods estimated from InSAR. Ito et al. (2015) used the digital elevation model (DEM) data obtained from the airborne laser scanning and flood inundation area recorded from the report to examine the relationship between land subsidence and floods in Japan. However, a major limitation by observation-driven approaches is that inundation is often captured via 'snapshots' without fully characterizing its temporal dynamics.

An alternative to remote sensing is to conduct hydrodynamic modeling of flood inundation. Hsu et al. (2010) utilized HEC-RAS 1D and FLO-2D models to analyze the influence of the land subsidence for flood hazards based on two designed flow rates with 1994 and 2004 DEM data. Yin et al. (2013) conducted a scenarios-based study using a 1D/2D coupled flood inundation model to investigate compound effects of land subsidence and sea level rise on fluvial flooding in Shanghai, China. Carisi et al. (2017) investigated the flooding intensity in Italy for four different terrain configurations using a hydrodynamic model which includes both 1D and 2D simulations. Dang et al. (2018) used the hydrodynamic model MIKE 11 to study the impact of land subsidence, sea level rise, and water infrastructure development in Vietnam based on some designed scenarios. Ouyang et al. (2020) applied MIKE models over two periods (before and after land subsidence caused by the Tohoku earthquake) to quantify the effects of land subsidence on the inundation areas in Japan. Hydraulic/hydrodynamic modeling approach provides significant advantages over remote sensing methods due to its ability to capture the flood dynamics spatially and temporally.

Nonetheless, both remote sensing and hydrodynamic approaches to quantify the effects of land subsidence on flood inundation heavily rely on the surveyed DEM (Hsu et al., 2010; Ito et al., 2015; Carisi et al., 2017; Ouyang et al., 2020), field measurements/monitoring (Miller et al., 2008; Wang et al., 2012; Yin et al., 2013, 2016;), and remote sensing techniques (Dixon et al., 2006; Dang et al., 2018) to represent land subsidence information. The infrequent, short-duration, topology surveys/monitoring inevitably requires assuming a linear land subsidence at some constant rate, which could be unrealistic especially when the anthropogenic activities like groundwater pumping drive the land subsidence. Therefore, few attentions have been paid to quantifying the evolution of land subsidence influence on flood extent and depth over an extended historical period. This is largely due to the lack of reliable methods to realistically estimate land subsidence both continuously and at high spatial resolution.

To this end, our study investigates retrospective changes of regional topology due to 117 years (1900 to 2017) of land subsidence, which is enabled by a high-resolution, physics-based modeling of groundwater withdrawal and the consequent aquifer-system compaction. By analyzing the spatial heterogeneity of land subsidence and the consequent change over flood inundation using a hydrodynamic model in different historical periods, we have an unprecedented chance to better understand the complex of flood inundation and its relationship with land subsidence. The outcome of this study can help people better understand the dynamic evolvement of flood inundation due to land subsidence so that better planning can be initiated for sustainable urban development for coastal communities. Research objectives of this study are (1) to examine the change in topology due to a historical 117-year land subsidence, (2) to establish a hydrodynamic model that accurately reproduces the flood inundation of 2017 Hurricane Harvey, and (3) to investigate the change in Harvey flood inundation due to the historical land subsidence in Brays Bayou, Texas.

The rest of this paper is organized as follows: Section 2 introduces the study area and materials utilized including land subsidence data, DEM, channel bathymetry, precipitation, and observation data; Section 3 describes the methodology of model development, model calibration and validation, and designed simulation scenarios; Section 4 presents the results of the model simulations for different scenarios; Section 5 discusses the results, underlines the main findings and limitations in this study, and recommends future directions for other similar studies; The conclusions with insights gained from this study are summarized in Section 6.

2. Study area and materials

2.1. Study area

Harris County, located in the southeastern of Texas (Fig. 1a), has experienced tremendous increases in development in the past decades (Walker and Shelton, 2016; Chun et al., 2021). Owing to the rapid growth and groundwater withdrawal, land subsidence in this region has been occurring

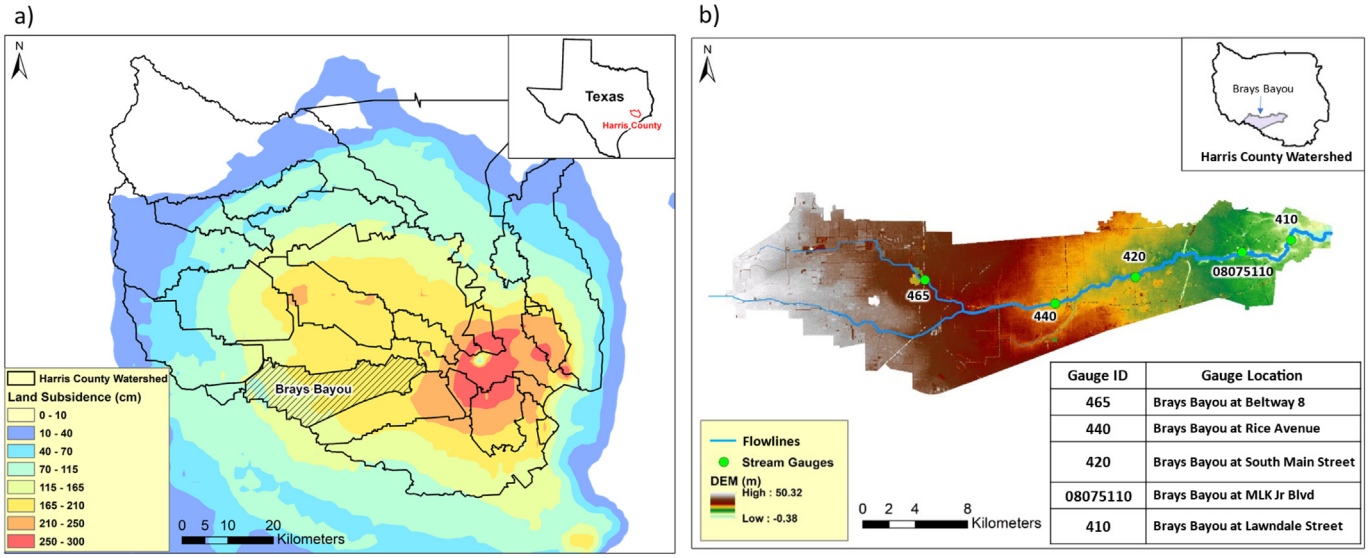

Fig. 1. (a) Location of the study area (Brays Bayou) with land subsidence during the period of 1900 to 2017 in Harris County and (b) Flowline, stream gauges and the digital elevation model (DEM) in Brays Bayou. Land subsidence due to groundwater withdrawal is simulated using the Houston Area Groundwater Model (HAGM).

for years (Kasmarek et al., 2009) and Fig. 1a shows the cumulative land subsidence simulated using the Houston Area Groundwater Model (HAGM, Kasmarek, 2013) from 1900 to 2017 in this region. Not only has the increased urbanization caused subsidence, but it also has aggravated this region's flood vulnerability (Garcia et al., 2020). From 1996 to 2019, there are over one hundred flood events that occurred in Harris County (FEMA), with about 10.3 billion US dollars of the total estimated losses to property damage (NOAA, 2020).

Located close to the land subsidence center (Fig. 1a), the Brays Bayou watershed is selected as the study area with a drainage area of approximately 330 km^2. 95 % of Brays Bayou is developed land (Fig. S1) and it is one of the most urbanized watersheds in Harris County (Bass, 2017; Gao et al., 2021). The climatology in this region is wet and subtropical with humid, hot summers and mild winters (Li et al., 2021). This area is vulnerable to floods due to its flat terrain, impermeable land surface (Fig. S2), clayey soil (Fig. S3), and frequent, extreme rainfall from tropical storms and hurricanes (Bedient et al., 2003; Bass et al., 2017; Li et al., 2021). Previous studies have shown that land subsidence made the overland and channel slopes flatter than 0.001 % downstream from Main Street to the East in Brays Bayou (Vieux and Bedient, 2004). Fig. 1b shows the Brays Bayou watershed with the digital elevation model (DEM) and five stream gauges.

2.2. Data

2.2.1. Land subsidence and topography data

In this study, land subsidence caused by groundwater withdrawal is simulated using the Houston Area Groundwater Model (HAGM) updated by Kasmarek (2013) with the Subsidence and Aquifer-System Compaction (SUB) package (Hoffmann et al., 2003). HAGM can simulate groundwater flow and land subsidence in the northern part of the Gulf Coast aquifer system in Texas from predevelopment (before 1891) through 2009. Land subsidence from 2009 to 2017 is simulated with HAGM by using the 2009 groundwater pumping plan of a total 3 million m^3/day since no significant primary compaction subsidence was observed during the stable groundwater level period in trend for the Chicot and Evangeline aquifers (Liu et al., 2019). As much as 3.05 m of land subsidence was observed in 1979 in the Houston-Galveston region as a result of inelastic compaction of aquitards in the Chicot and Evangeline aquifers between 1937 and 1979 (Galloway et al., 1999) and simulated subsidence up to 3.0 m (300 cm) can be found in Fig. 1a.

The spatial and temporal distribution of land subsidence rates from 1900 to 2017 in the Brays Bayou watershed can be seen in Figs. S4a-S4f (Supplementary Materials). No significant subsidence is found for the period of 1900 to 1930 in the study area (Fig. S4a). Then the preconsolidation pressure heads within the Chicot and Evangeline aquifers continuously reacted to lowering groundwater levels, which in turn was caused by continuously increasing groundwater withdrawal rates from 0.57 to 4.28 million m^3/day by 1979 (Liu et al., 2019). Figs. S4b, S4c and S4d show simulated subsidence rates up to 40 to 55 mm/year in a small border area during 1930 to 1960, up to 40 to 55 mm/year in an extended area during 1960 to 1970, and up to 75 to 95 mm/year in a big central area during 1970 to 1980. This land subsidence occurred without any management over groundwater levels before 1979. However, it is found that the management of recovering groundwater levels in the Galveston-Houston region from 1979 to 2000 (Kasmarek, 2013; Liu et al., 2019) successfully decreased inelastic primary compaction from up to 79 to 95 mm/year due to increasing groundwater withdrawals from 2.5 to 4.3 million m^3/day during 1970 to 1980 (Fig. S4d) down to up to 40 to 55 mm/year due to decreasing groundwater withdrawals from 4.3 to 3.5 million m^3/day during 1980 to 1990 (Fig. S4e) and further down to <5 mm/year with some land rebound (less than zero mm/year) through further decreasing groundwater withdrawals from 4.3 to 3.0 million m^3/day during 1990 to 2017. Land subsidence rates of 0.08 to 8.49 mm/year since 2005 observed by 13 borehole extensometers is due to creep compaction of the Gulf Coast aquifer system (Liu et al., 2019), which is out of simulated subsidence only due to groundwater pumping (Kasmarek, 2013). Overall, land subsidence increases rapidly, especially from 1960 to 1970 with the mean areal rate of 38.2 mm/year and from 1970 to 1980 with the mean areal rate of 58.8 mm/year. Then the land subsidence rate almost stopped increasing after 1980 and ended with the rate of 1.9 mm/year during the period of 1990 to 2017.

DEM with 10-m spatial resolution is obtained from the USGS website (https://apps.nationalmap.gov/downloader/#/). Since DEM cannot represent sufficient information on channel cross-sections, bathymetry data needs to be combined with DEM if available to better represent channel shape (Goodell, 2014). In this study, channel bathymetry data is obtained from the Model and Map Management (M3) system (HCFCD, 2020a).

2.2.2. Precipitation and observation data

Precipitation data used in this study is the hourly Stage IV product with 4-km spatial resolution obtained from the National Centers for Environmental Prediction (NCEP), which combines multi-sensor (quality-controlled radar, satellite, and rain gauge) precipitation estimates (Lin and Mitchell, 2005; Habib et al., 2009; Nelson et al., 2016). The Stage IV radar data

during Hurricane Harvey have been systematically validated by Gao et al. (2021) and showed close match with ground truths from a dense rain-gauge network.

Observational stage hydrographs at five (5) stream gauges (Fig. 1b) are retrieved from the Harris County Flood Warning System website (HCFCD, 2020b). Except the most downstream gauge which is used as the downstream boundary condition for the hydrodynamic model, the rest four stream gauges are utilized as benchmarks to calibrate the model in this study. Ninety-nine (99) highwater marks surveyed during the 2017 Hurricane Harvey are obtained from the Harris County Flood Control District (HCFCD, 2020c) and this information is used to validate the model simulation.

3. Methodologies

3.1. Terrain data preparation

Since the year of 2017 is selected as the starting point, the 2017 terrain data is developed by combining the DEM of 2017 with channel bathymetry in RAS Mapper. Then terrain data of other years (1900, 1930, 1945, 1960, 1970, 1980, 1990, 2000, 2010) are developed using the projected land subsidence of that year superimposed upon the 2017 condition as shown in Eq. (1) below:

$$T_Y = T_{2017} + LS_{Y\text{-}2017} \quad (1)$$

where T means Terrain, LS is Land Subsidence, and Y is year.

3.2. Model set-up, calibration, and simulation scenarios

In this study, the Hydrologic Engineering Center-River Analysis System 2D (HEC-RAS version 5.0) is utilized as a modeling tool to simulate the flood inundation due to its broad applications in both industrial and academic fields (e.g., Tayefi et al., 2007; Shustikova et al., 2019; Costabile et al., 2020; Ongdas et al., 2020; Shrestha et al., 2020; Karim et al., 2021). HEC-RAS 2D solves either the two-dimensional Saint Venant equations (with optional momentum additions for turbulence and Coriolies effects) or the diffusion wave equations (Brunner et al., 2016a, 2016b). Fig. 2 illustrates the input data and workflow of the model set-up and simulations.

The HEC-RAS 2D model is built by first importing the prepared terrain data (DEM combined with channel bathymetry) into the RAS Mapper. A 2D flow area with grid dimensions of 30-m × 30-m is then created as a computational mesh, and this cell size is selected in respect to computation time and model stability. The Manning's roughness is assigned based on the land use and land cover data from the 2016 National Land Cover Database (NLCD, https://www.mrlc.gov).

To provide precipitation input, we process the hourly Stage IV rainfall by calculating the areal average values over the watershed (Fig. S5a) since the HEC-RAS (version 5.0) only accepts a time series of spatially uniform precipitation as input. The total rainfall from Harvey (Fig. S6) shows little spatial variability with the coefficient of variation being 0.05 for Stage IV rainfall values within the watershed boundary. Therefore, we consider it acceptable to adopt the watershed-averaged precipitation for HEC-RAS input. Another limitation of HEC-RAS v 5.0 is the inability to represent infiltration. For Hurricane Harvey, Gao et al. (2021) estimated the runoff coefficient in Brays Bayou to be 91 % based the runoff volume received by the most downstream USGS gauge and total rainfall, which is largely due to the 95 % urbanization rate and 72 % imperviousness of Brays Bayou as well as the enormous rain volume from Hurricane Harvey. Given the high runoff coefficient, neglecting loss caused by infiltration and interception is also considered reasonable in this study.

The stage hydrograph, as shown in Fig. S5b at gauge 410 (Fig. 1b), is utilized as the downstream boundary condition for the unsteady simulation. Additionally, an initial condition with ramp-up option is set in order to let the flow go through the 2D area and establish the initial wet conditions before the beginning of the simulations. Detailed model specification can be found in Table 1.

To consider the land subsidence, the authors build respective HEC-RAS 2D models to represent the corresponding topography from 1900 to 2017 through modifications of terrain data. The model of 2017 is manually calibrated for Hurricane Harvey (8/25/2017-8/30/2017) by comparing the simulated and observed stage hydrographs at four-gauge locations (gauges 465, 440, 420, and 08075110). The Manning's roughness coefficients are modified via a uniform multiplicative factor during the calibration process.

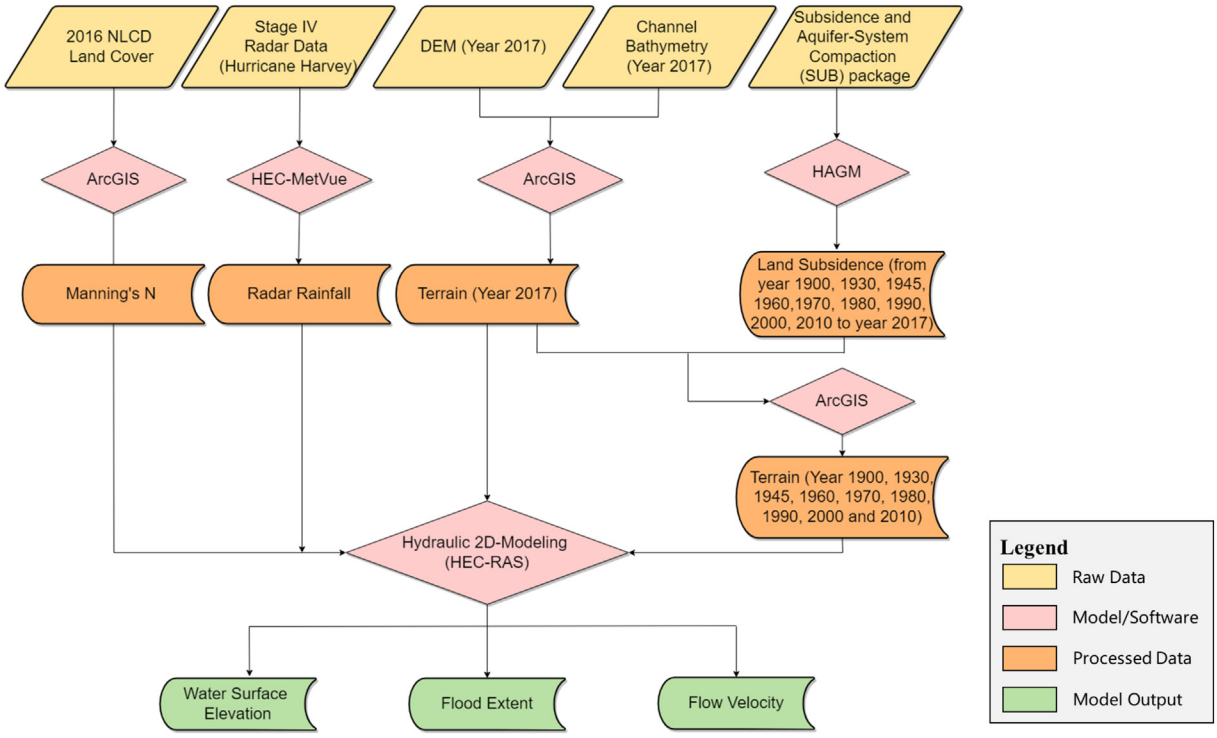

Fig. 2. Overarching flowchart of model set-up and simulations.

Table 1
HEC-RAS 2D model settings.

Parameters	Settings
Boundary Conditions	Rainfall and downstream stage hydrograph
2D Flow Equation Set	Diffusion Wave
Maximum Iterations	20
Initial Conditions Ramp up Time (hrs)	120
Boundary Condition Ramp Up Fraction	0.5
Model Computation Interval	3-min
Model Output Interval	15-min

Once the calibration is satisfactory, we use 99 surveyed highwater marks during Hurricane Harvey to validate the calibration results. After the model calibration and validation, the optimized Manning's roughness is implemented for models of other years between 1900 and 2017. Thus, each simulation scenario has the same model settings except the associated terrain to represent only the impacts caused by the land subsidence.

3.3. Quantitative statistics

Calibration results are evaluated using the root mean squared error (RMSE), Nash-Sutcliffe Efficiency (NSE), and correlation coefficient (CC). RMSE describes the discrepancy between the simulation and observation, quantifying the scale of the error (Mediero et al., 2011). The closer the RMSE value to 0, the more accurate the model is. While NSE shows how well the plot of observation results versus the simulation fits the 1:1 diagonal line. The higher NSE value is, the better the simulation performance (Legates and McCabe, 1999). CC measures the linear correlation between simulation and observation. Because in this study we intend to analyze the maximum flood inundation, the absolute error at the flood peak timing is evaluated. The equations of computing RMSE, NSE, CC, and absolute error at peak timing are shown in Eqs. (2)-(5):

$$RMSE = \sqrt{\frac{\Sigma_{i=1}^{n}\left(H_{sim}^{i} - H_{obs}^{i}\right)^2}{n}} \tag{2}$$

$$NSE = 1 - \frac{\Sigma_{i=1}^{n}\left(H_{sim}^{i} - H_{obs}^{i}\right)^2}{\Sigma_{i=1}^{n}\left(H_{obs}^{i} - \overline{H_{obs}}\right)^2} \tag{3}$$

$$CC = \frac{1}{n-1}\Sigma_{i=1}^{n}\left(\frac{H_{sim}^{i} - \mu_{sim}}{\sigma_{sim}}\right)\left(\frac{H_{obs}^{i} - \mu_{obs}}{\sigma_{obs}}\right) \tag{4}$$

$$Absolute\ Error = |H_{sim}^{peak} - H_{obs}^{peak}| \tag{5}$$

where H_{sim}^{i} is the simulated flood depth of the ith data, H_{obs}^{i} is the observed flood depth of the ith data, and $\overline{H_{obs}}$ is the mean of the observed flood depth. μ_{sim} and σ_{sim} are the mean and standard deviation of simulated data, respectively. μ_{obs} and σ_{obs} are those of observation, and n is number of the total data points. H_{sim}^{peak} and H_{obs}^{peak} are the simulated and observed flood depth at peak timing, respectively.

To compare the changes in maximum flood depth caused by the land subsidence, the authors calculate the flood depth difference (FDD) by subtracting the maximum flood depth simulated using the scenario for 1900 from the maximum flood depth simulated from other years (e,g, year Y). Since the 1900 scenario is the baseline flood condition without land subsidence, the subtrahend is always the maximum flood depth in the Year 1900 for this quantification, as shown in Eq. (6) below:

$$FDD = D_{sim}^{Y} - D_{ref}^{1900} \tag{6}$$

where D_{sim}^{Y} is the simulated flood depth in year Y and D_{ref}^{1900} is the reference flood depth in 1900. The positive FDD means the maximum flood depth in year Y is deeper than the baseline condition (1900), indicating the adverse impacts caused by the land subsidence between 1900 and year Y. A negative value of FDD means the maximum flood depth in year Y is smaller than the year 1900.

After simulating all scenarios, two indices are calculated to analyze the temporal difference in flood inundation results, which are Fit Statistic and Root Mean Square Deviation (RMSD). The Fit Statistic exhibits the inundated areas of simulation as a fraction of the reference, which represents a meaningful assessment of the inundation extents (Bates and De Roo, 2000; Yin et al., 2016; Rajib et al., 2020). The metric is calculated as follows:

$$Fit = \frac{A_o}{A_r + A_s - A_o} \tag{7}$$

where A_o refers to the overlapped inundated area of the reference and simulation, A_r refers to the reference inundated area (in this case the reference is the inundated area in 1900) and A_s refers to area of simulated flood extent. The Fit index ranges from 0 if none of the simulated areas matches the reference to 1 for a perfect fit.

The RMSD compares flood depth between simulated results and the reference upon a cell-by-cell basis (Yu and Lane, 2011; Grimaldi et al., 2019). It is calculated as in the following Eq. (8):

$$RMSD\ (depth) = \sqrt{\frac{\Sigma_{i=0}^{n}\left(D_{sim}^{i} - D_{ref}^{i}\right)^2}{n}} \tag{8}$$

where D_{sim}^{i} and $D_{ref}^{i}$are the simulated and reference flood depth of the ith cell, and n is the number of inundated cells.

4. Results

4.1. Model calibration and validation

The calibration results for Hurricane Harvey (Table 2) show a good fit between the simulated and observed with CC larger than 0.9 and NSE higher than 0.8 at four gauges. The comparisons of stage hydrographs can be found in Fig. S7 (Supplementary Materials).

Fig. 3a shows the locations of the surveyed highwater marks used for validation. The comparison between the observed and simulated is presented in Fig. 3b. Overall, the correlation of determination of 0.95 between the simulated flood depths and highwater marks indicates that the model is reliable to reproduce the flood depth well and allows us to further investigate the impacts of land subsidence on flood inundation.

4.2. Spatial-temporal patterns of maximum flood extent and depth

Examining the spatial and temporal patterns of the maximum flood extent and flood depth allows the authors to identify varying degrees of the impacts of land subsidence on flood inundation in the study area. The simulated results from the calibrated HEC-RAS 2D model for the maximum flood depth based on the topography of 1900 and 2017 are shown in Fig. 4a and b, respectively. To decipher the changes of the corresponding flood inundation with respect to the impacts from the land subsidence, the authors calculate the flood depth difference (FDD) between 2017 and 1900 (Fig. 4c), alongside land subsidence contours for the corresponding years (Fig. 4d). Overall, the spatial patterns of changes in flood depth are

Table 2
Statistics of calibration results at four stream gauges along Brays Bayou.

Gauge ID	RMSE (m)	NSE	CC	Absolute Error at Peak Timing (m)
465	0.87	0.84	0.95	0.28
440	1.11	0.81	0.90	0.44
420	0.99	0.87	0.94	0.40
08075110	1.07	0.88	0.94	0.36

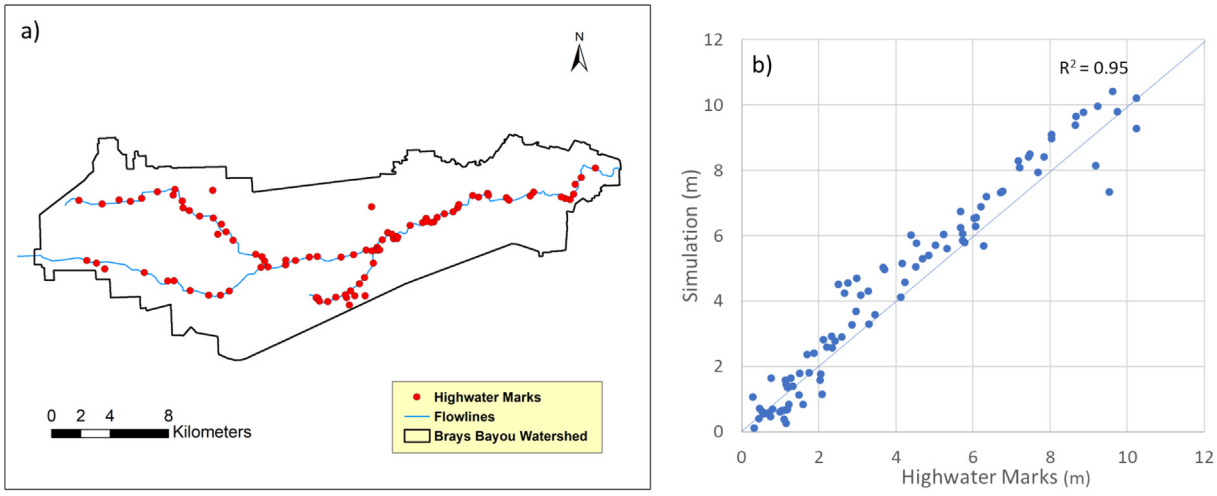

Fig. 3. (a) Highwater marks in the Brays Bayou watershed and (b) Comparison of the surveyed and simulated water depth of Hurricane Harvey.

found to be consistent with land subsidence. For example, compared to the simulated flood depth under the 1900 condition, the areas within Zones A and B are observed with much deeper water under the 2017 condition, which coincides with the higher subsidence found locally in those areas (Zones A and B).

In addition, the spatial differences in maximum flood depth between the baseline condition (1900) and the subsequent years (1960, 1970, 1980, 1990) for Hurricane Harvey are also calculated, as shown in Figs. 5a to h. The substantial changes in flood depth can be identified near the subsidence centers (labeled as Zone A in Figs. 5a to h, Zone B in Fig. 5e to h) for various time periods. From the time-series of change in land subsidence, as shown in Fig. 5b, d, f, and h, one can see that the land subsidence started from the downstream to upstream sections of the watershed with non-uniform subsidence rates. It is found that the changes in flood depth within Zone B became significant after 1980 (Fig. 5e and g), which corresponds well with the larger land subsidence occurring in midstream (Fig. 5f and h).

Besides assessing spatial changes in land subsidence and flood depth individually, an evaluation of the relationship between FDD and land subsidence from 1900 to 2017 is also conducted. Fig. 6 illustrates the ratio of the flood depth difference (FDD) to land subsidence in the period 1900 to 2017. It can be found that the highest ratio of FDD over land subsidence is about 10 %, indicating that the flood impacts caused by land subsidence are relatively minor compared to the magnitude of land subsidence itself. For example, the maximum land subsidence can reach approximately 2-m, while the changes in flood depth are significantly less with 12 cm at the same location.

Table 3 quantifies and summarizes the area and percentage changes in FDD for different time periods, in which the negative value of FDD refers to a decrease in maximum flood depth compared to the year 1900. The results

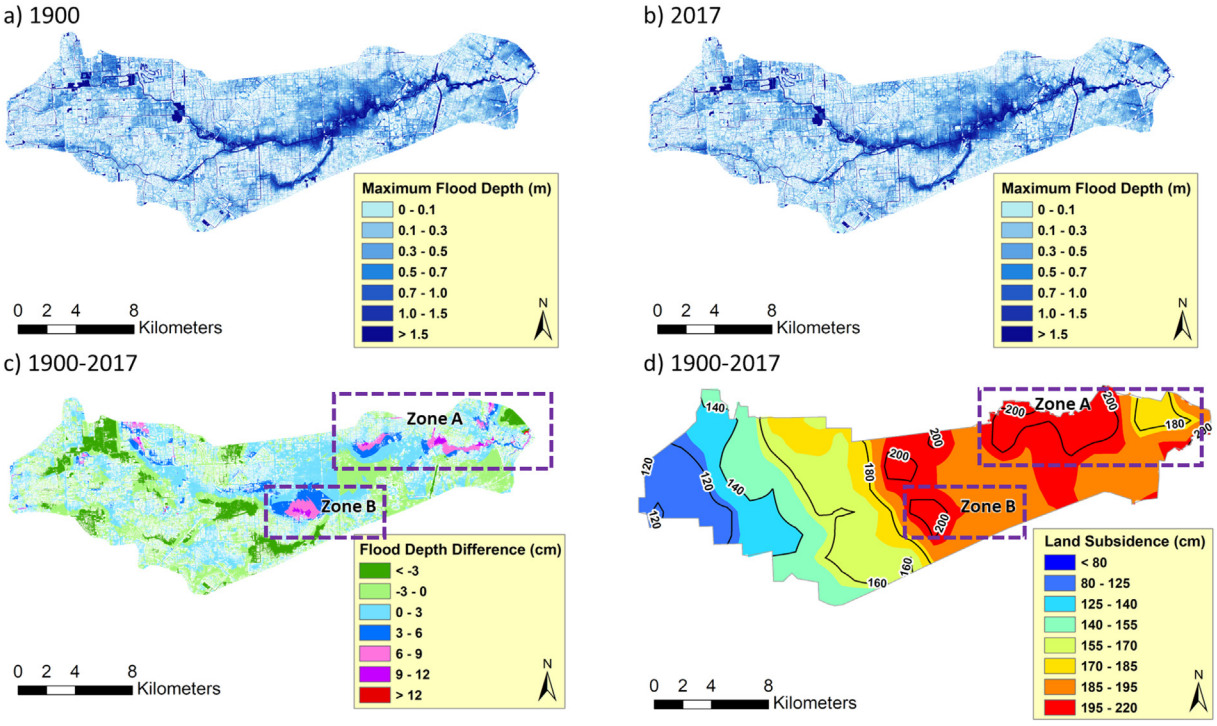

Fig. 4. (a) Maximum flood depth in 1900, (b) Maximum flood depth in 2017, (c) Flood depth difference (FDD) between 1900 and 2017, and (d) Land subsidence contours in the period of 1900 to 2017.

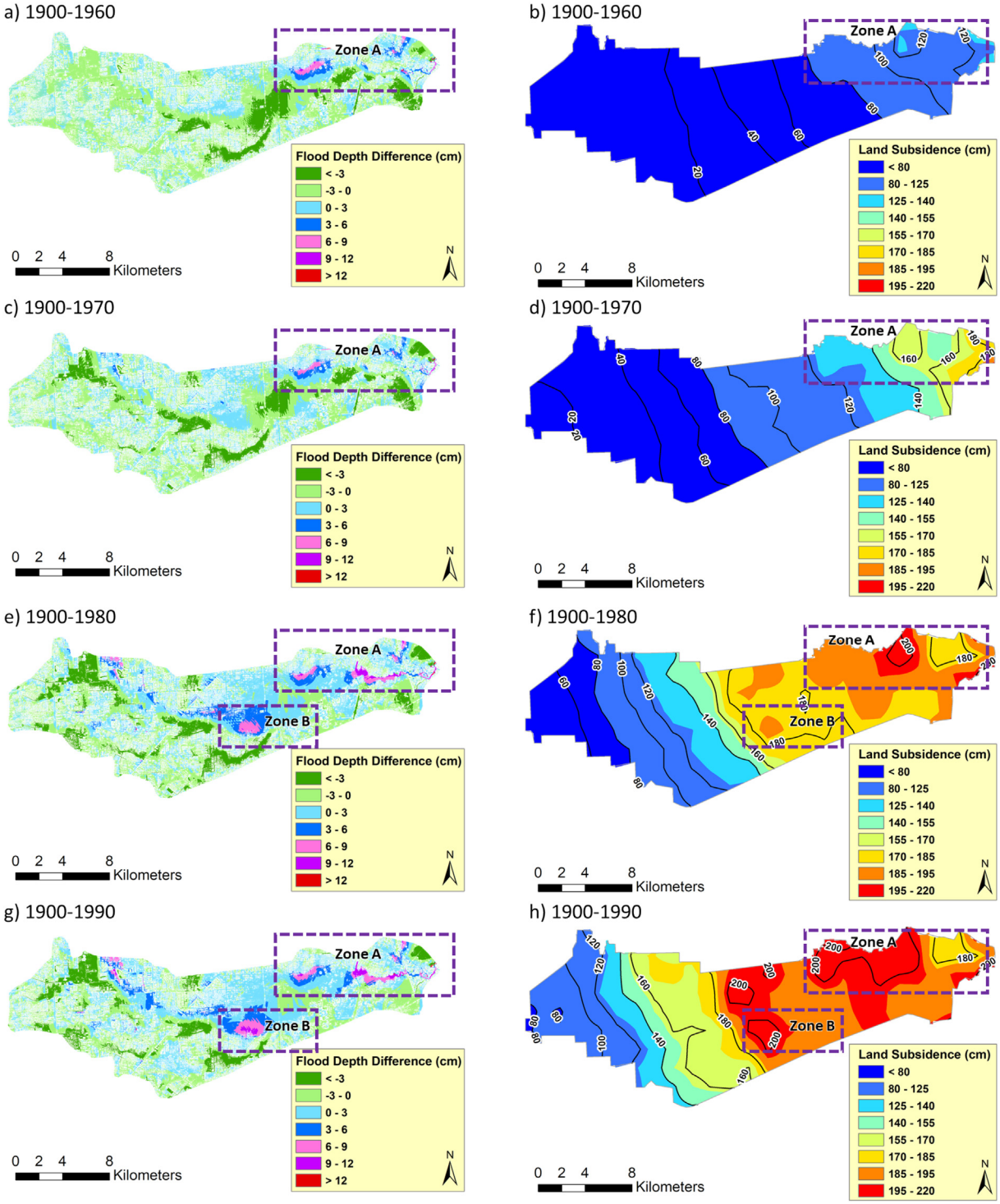

Fig. 5. (a) Flood depth difference (FDD) between 1900 and 1960, (b) Land subsidence contours in the period of 1900 to 1960, (c) FDD between 1900 and 1970, (d) Land subsidence contours in the period of 1900 to 1970, (e) FDD between 1900 and 1980, (f) Land subsidence contours in the period of 1900 to 1980, (g) FDD between 1900 and 1990, and (h) Land subsidence contours in the period of 1900 to 1990.

demonstrate that land subsidence may bring beneficial impacts with negative FDD for at least 48 % of the total inundated area of all six scenarios. In 1930 when land subsidence had just started, beneficial impacts could be found for 87 % of the total inundated area with negative FDD. The reason could be that minor land subsidence may help flood water drain faster downstream, resulting in shallower water depth for some places within the watershed. Areas with the increased FDD (0 to 9 cm) constitute only 13 % of the study domain in the period 1900 to 1930, then account for approximately 34 %, 37 %, 49 %, and 51 % in 1960, 1970, 1980, and 1990 respectively. It can be seen that major changes of FDD happened between 1970 and 1980 (37 % to 49 %), which corresponds the same period with the largest land subsidence rate (Fig. S4d). The areas with relatively large flood depth difference (>9 cm) make up the rest 1 % at most in the period of 1900 to 1990.

Table 3. Changes of flood depth difference (cm) in the area (km^2) and percentage (%) of the simulation domain for various time periods.

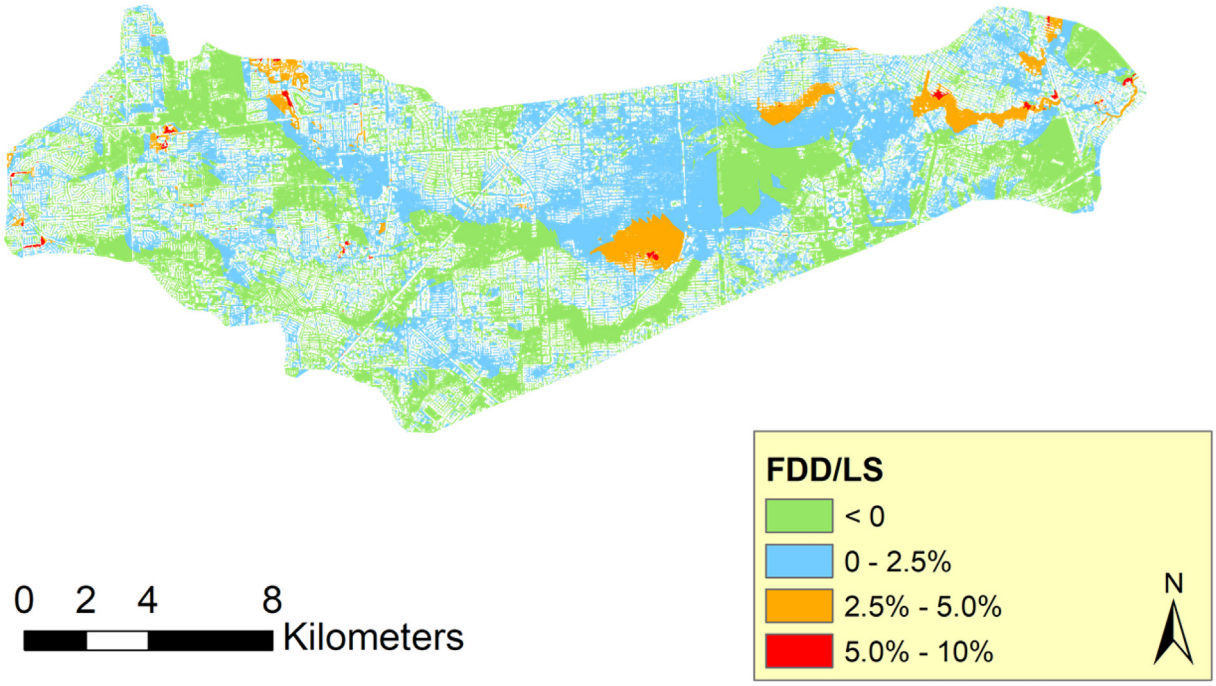

Fig. 6. Ratio of the flood depth difference (FDD) to land subsidence in the period of 1900 to 2017.

Fit statistics and RMSD of flood depth for various scenarios using the 1900 condition as baseline are determined and presented in Fig. 7a and b, respectively. The Fit value indicates how similar two inundation areas are. Fig. 7a shows that the land subsidence does have an influence on the extent of the inundated area, yet the changes appear to be limited since the values are always above 0.97. RMSD measures the difference in flood depth on a cell-by-cell basis between simulated results and reference. Fig. 7b shows that compared to the 1900 condition, flood depth increases starting from 1930 and reaches its climax in 1980, followed by a plateau. These two indices (Fit and RMSD) demonstrate a similar trend in terms of inundation extent and flood depth, and the rapid changes in Fit and RMSD values between 1970 and 1980 coincide with the fast rate of land subsidence of the same time period as illustrated in Fig. S4d.

Fig. 7c presents the temporal changes of the area in terms of flood depth difference (FDD). The blue bars represent the total inundated areas, and no significant changes are found over the years, indicating the impact of land subsidence on flood extent is minor in this study. The green and red bars represent the area of grids where the FDD is negative and positive, respectively. The area with positive and negative FDD show opposite trends over the years: the area with negative/positive FDD (green/red bars) tends to decrease/increase rapidly before 1980 and become stable after 1980. Areas with negative FDD (green) represent places that gain benefits from the land subsidence compared to the baseline condition (1900), and the benefit diminishes as land subsidence gets worse. To better quantify the relative area changes in FDD, the authors further calculate percentages of positive and negative FDD as shown in Fig. 7d. Both percentages of positive and negative FDD show steeper slopes during 1970 to 1980 than any other decades, which displays an agreement with the previous results of having the largest land subsidence rate between the same period (Fig. S4d). After 1980, these two percentages begin to stabilize due to the deceleration in land subsidence. Overall, the results imply that land subsidence has little impact on causing the change of flood inundation areas but does have an impact on the change of flood depth.

4.3. Sectional analyses of flood inundation

To further evaluate the spatial and temporal patterns of flood inundation at a local scale, the authors divide the Brays Bayou watershed into three sections: upstream (123.7 km^2) from its headwater to S. Gessner Rd., midstream (97.3 km^2) from S. Gessner Rd. to Main St., and downstream (56.9 km^2) of Main St. (Fig. 8a) (Bedient et al., 2002). Fig. 8b shows the temporal changes in median values of FDD for the upstream, midstream, and downstream sections. It can be found that median values show a decreasing trend from 1930 to 1945 in all three sections with negative FDD, indicating that flood water in these years is shallower than that in 1900 condition. Median values of FDD at the downstream section start to increase since 1945 and become stable after 1980. Median values of FDD in the midstream section are observed to increase from 1960 and reach to their highest in 1980. Overall, median values of the upstream, midstream, and downstream sections show similar trends among years

Table 3
Changes of flood depth difference (cm) in the area (km^2) and percentage (%) of the simulation domain for various time periods (Pct means Percentage).

Flood depth difference (cm)	1900–1930		1900–1960		1900–1970		1900–1980		1900–1990		1900–2017	
	Area (km^2)	Pct (%)	Area (km^2)	Pct (%)	Area (km^2)	Pct (%)	Area (km^2)	Pct (%)	Area (km^2)	Pct (%)	Area (km^2)	Pct (%)
< −3.0	0.09	0.05	23.04	12.55	27.96	15.25	26.85	14.68	22.37	12.21	20.8	11.35
−3.0–0.0	160.82	86.84	98.17	53.47	86.86	47.37	65.67	35.91	65.34	35.66	68.22	37.23
0.0–3.0	24.17	13.05	56.89	30.99	63.49	34.62	70.9	38.77	74.75	40.8	75.98	41.46
3.1–6.0	0.07	0.04	3.82	2.08	4.01	2.19	13.4	7.33	13.39	7.31	11.33	6.18
6.1–9.0	0.02	0.01	1.46	0.8	0.94	0.51	4.82	2.64	5.59	3.05	5.77	3.15
9.1–12.0	0.01	0.01	0.15	0.08	0.07	0.04	1.15	0.63	1.71	0.93	1.07	0.58
>12.0	0.02	0	0.07	0.03	0.03	0.02	0.07	0.04	0.07	0.04	0.09	0.05

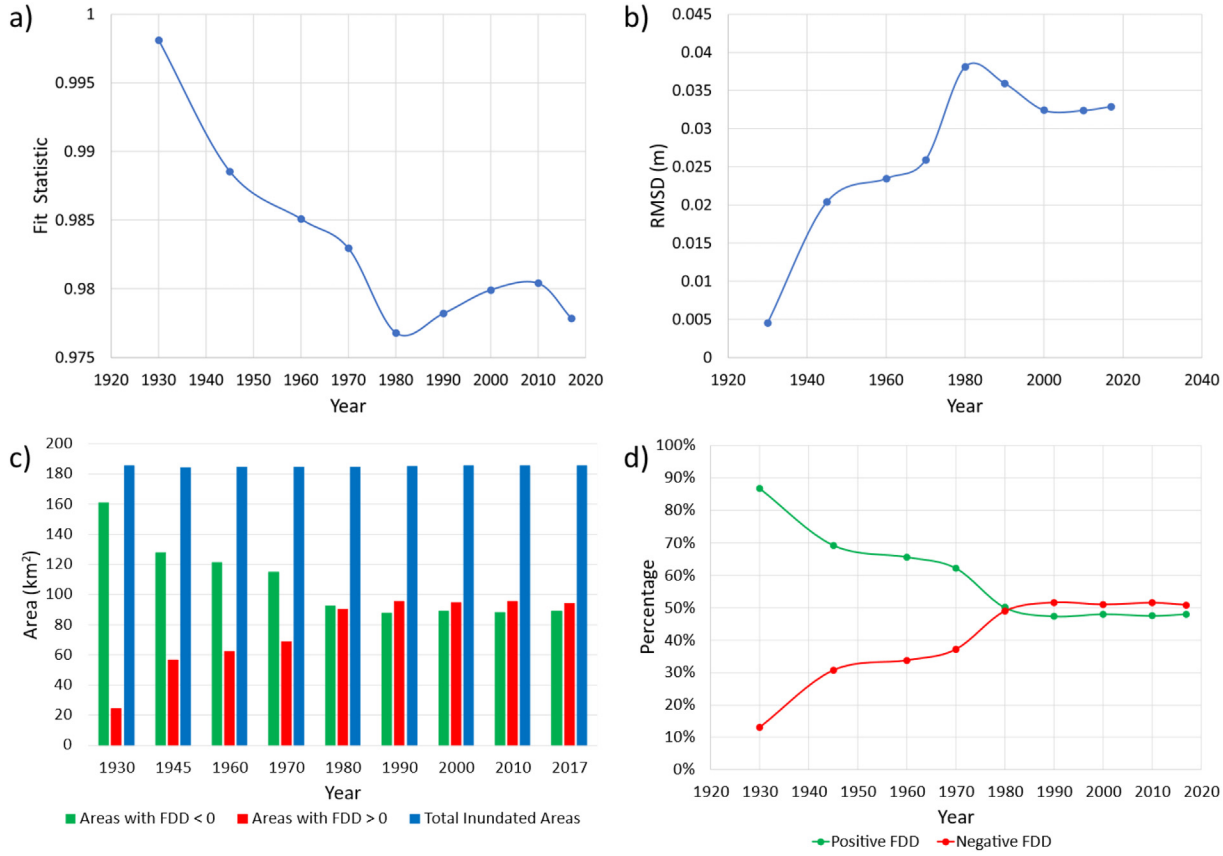

Fig. 7. (a) Trend of the Fit Statistics of inundation area, (b) Trend of the flood depth RMSD, (c) Bar chart of inundation area changes, and (d) Trends of percentages of positive and negative flood depth difference (FDD).

(first decrease and then increase) while the time of turning points varies. This may be associated with the non-uniform changes of land subsidence in various locations. As shown in Table 4, the midstream section features the highest annual subsidence rate during 1970 to 1980, consequently the median value of FDD in midstream shows the largest increase (from −0.26 cm to 0.45 cm) than those in the other two sections. After 1990, median values of FDD in all sections show minor changes, corresponding to the decreasing land subsidence rate at the same time (Table 4).

A similar analysis is also conducted for the maximum flow velocity ratio (FVR) in the upstream, midstream, and downstream sections of Brays Bayou. FVR is calculated by taking the maximum flow velocity simulated in 1900 and other years (e.g., the year 2017) as denominator and numerator, respectively. As shown in Fig. 8c, median values of FVR in all three sections show an increasing trend from 1930 to 1970, while FVR in midstream increases faster than up- and downstream sections. Overall, the changes of FVR in upstream show some latency. In other words, the median value in upstream always reaches its climax/dip later than those of the other two sections. These findings further suggest that land subsidence contributes to the change of flood depth and flow velocity at different sections with variant patterns, resulted from the non-uniform land subsidence rates over the Brays Bayou watershed.

5. Discussions

Our results indicate that land subsidence in general has a relatively minor influence on flood inundation compared to the magnitude of land subsidence itself. As shown in Fig. 6, the ratio of positive FDD values to corresponding land subsidence is mostly from 0 to 5 %, with the highest being about 10 %, This finding is similar with Yin et al. (2016), where their results show that the change in inundation depth is about 10 % of the magnitude of land subsidence. Also, we find that flood water is deepened in places featuring evident land subsidence at a local scale. As illustrated in Fig. 4, changes of flood depth in Zone A and Zone B are higher than in the surrounding areas. Similar findings are also reported by Hsu et al. (2010) and Ito et al. (2015). Hsu et al. (2010) found that areas with serious land subsidence have increased inundation depth based on hydrodynamic modeling with hypothetical design flow rates. Ito et al. (2015) analyzed three flood events (occurred in 1970, 2004, and 2013) and concluded that water tends to accumulate in the area surrounded by slightly highlands (relative elevation +1–2 m).

In our analyses, some unique characteristics in the flood inundation are revealed due to the spatial heterogeneity and decadal evolution of land subsidence, which would otherwise be prohibited using traditional methods (e.g., surveyed DEM, field measurements/monitoring, remote sensing) to represent land subsidence. First, the effects of land subsidence are not only heterogeneous but even mixed with coexisting positive and negative impacts on flood inundation (Figs. 5, Fig. 7c and d). The spatial heterogeneity is also reported by Yin et al. (2016), where they found land subsidence may have a non-linear impact on flooding. This is mainly due to the non-uniform rates of land subsidence between different time periods (Fig. S4). In 1930, approximately 88 % of inundated area features negative FDD compared to 1900 baseline condition (Fig. 7c), indicating most places actually gain benefits from land subsidence. As illustrated in Fig. 7d, these benefits (green line) decline as land subsidence continues increasing until 1980. Percentages of negative (green line) and positive (red line) FDD intersect 1980, which marks a turning point when adverse impacts on flood depth caused by land subsidence outweigh the benefits in the study region. After 1980, land subsidence slows down and tends to cease, causing the areas with positive and negative impacts to stabilize till the present.

Second, the decadal evolution of land subsidence exerts cumulative effects on flood inundation, where previous land subsidence hotspots could

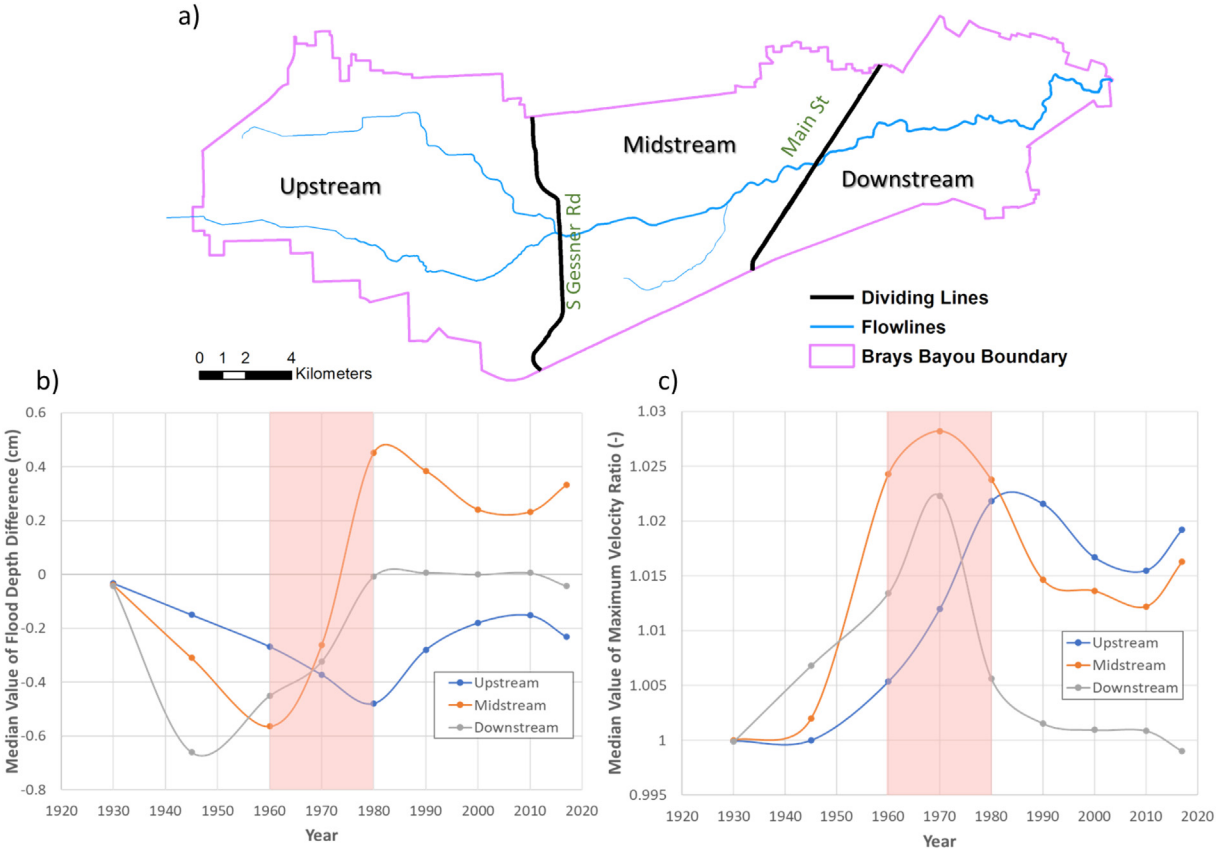

Fig. 8. (a) Example map of dividing the Brays Bayou watershed into three sections, (b) Median values of the flood depth difference (FDD), and (c) median values of the flood velocity ratio (FVR) for upstream, midstream, and downstream sections. Red shaded area represents the period with the largest land subsidence rate (1960–1980). (For interpretation of the references to colour in this figure legend, the reader is referred to the web version of this article.)

be altered by later continuing land subsidence, i.e., emergence of new land subsidence hotspots in the watershed. As shown in Fig. 5, we can find that land subsidence hotspots have been drifting from downstream towards upstream over time, causing previously impacted areas to 'recover and even benefit'. From analyses of three sections (up-, mid-, and downstream) in Brays Bayou, flooding condition in midstream are the worst after 1970, where the median value of FDD is higher compared to the up- and downstream sections (Fig. 8b). The reason is that when the new land subsidence hotspot appeared at midstream, flood water generated from upstream would accumulate and be held locally before flowing downstream. Unique from any other previous studies, the sectional evaluation reveals the locally deepened flood inundation and accelerated flood waves near the main channel, which could be overlooked if only the net impact (aggregated over the watershed) were considered.

Finally, the way land subsidence affects flood inundation in this study sharply contrasts how coastal inundation is exacerbated by land subsidence (e.g., Shirzaei and Bürgmann, 2018; Catalao et al., 2020). For instance, the future 100-yr inundation maps estimated by Shirzaei and Bürgmann (2018) showed that land subsidence would amplify flood risk up to 90 % compared with scenarios only considering the sea level rise. Catalato et al. (2020) compared DEM with the sum of tide height, sea level rise, and cumulative land subsidence and estimated 25 % increase in flood area for future scenarios. In contrast, flood inundation areas simulated in this study for different years do not show significant changes due to land subsidence (blue bars in Fig. 7c), while areas with positive and negative FDD internally vary throughout years. The reason is that flood inundation is dynamic due to the movement of flood wave, while coastal inundation is static and controlled by the elevation difference between land and sea. This explains our findings where certain levels of land subsidence could reduce overland flood depth by accelerating flood velocity, whereas worse coastal inundation is almost definite given land subsidence (Wang et al., 2012; Yin et al., 2013; Shirzaei and Bürgmann, 2018; Catalao et al., 2020).

Table 4
Average annual land subsidence rate (mm/yr.) for the up-, mid-, and downstream sections in Brays Bayou during different time periods.

Time range	Upstream	Midstream	Downstream
1900–1930	0.0114	0.0133	0.0153
1930–1960	3.0435	17.2324	33.1066
1960–1970	28.6643	43.9189	44.7039
1970–1980	54.8193	73.9991	42.3358
1980–1990	36.0366	18.8718	6.1340
1990–2017	5.0227	0.0275	−0.1547

This study demonstrates the capability of HEC-RAS 2D for modeling the changes of flood inundation caused by land subsidence. However, due to some limitations related to the model itself (HEC-RAS version 5.0), the uniform rainfall is applied, and infiltration is neglected by our simulation, as explained before in detail (Section 3.2). These limitations/assumptions, though acceptable in this study, might be problematic for a different study region or storm events. As a remedy, newer versions of HEC-RAS will allow spatially varied precipitation as input as well as more realistic representation of the infiltration process, which is promising for broadening the applicability of our approaches (Brunner, 2021). Additionally, previous studies have reported sea level rise exacerbates coastal flooding, as another major contributor (besides land subsidence) to the total relative elevation difference between land and sea (Wang et al., 2012; Dang et al., 2018; Zeiger and Hubbart, 2021; Zhao et al., 2021; El Shinawi, 2022). Therefore, one clear future direction is to incorporate sea level rise into the analysis framework of this study. We expect storm surge, as another hazard from tropical cyclones, will be aggravated by sea level rise and

jointly impact a coastal region along with the rainfall-induced inland flooding.

6. Conclusion

This study provides fresh insights on the impact from land subsidence on flood inundation, which is uniquely enabled by a retrospective, 117-year, physics-based modeling by Liu et al. (2020) considering groundwater withdrawal and the consequent aquifer-system compaction. Hydrodynamic simulation of flood inundation from Hurricane Harvey over the topologies in different historical times from 1900 to 2017 depicts realistic pictures of how Harvey flood could have evolved over the 117 years due to continuous land subsidence in Brays Bayou, Texas. This research is among the first to shed light on the consequence of land subsidence on flooding that is continuous both in space and time.

Specifically, our results show that the overall change of flood depth caused by land subsidence is relatively minor compared to the magnitude of land subsidence itself. Over the course of 117 years, the worst impacted location in Brays Bayou experiences only 12 cm deepened flood water due to approximately 2-m subsidence at the same location. However, the impact from land subsidence on flood depth is non-linear in time, where effects from previous land subsidence hotspots could be altered by later continuing land subsidence, i.e., emergence of new land subsidence hotspots in the watershed. Specifically in Brays Bayou, later-occurring subsidence in upstream counteracts the preceding downstream subsidence, mitigating previously increased flood depth. Spatially, change in flood depth due to the land subsidence is not only heterogeneous but also mixed with coexisting deeper and shallower flood water. Land subsidence could reduce flood depth but accelerate flood velocity locally, while causing flood water to pond in other locations, e.g., lower main stem with mild slope.

The analyses established in this study can be replicated and expanded to regions with land subsidence and flooding issues. With the ongoing sea level rise due to a warming climate, the outcome of this research promises to enhance preparedness and resilience of coastal communities against future flooding hazards.

CRediT authorship contribution statement

Han Jiang: Conceptualization; Data curation; Investigation; Methodology; Software; Validation; Formal analysis; Writing-original draft, Reviewing and Editing

Jiaqi Zhang: Conceptualization; Data curation; Investigation; Methodology; Software; Validation; Formal analysis; Writing-original draft, Reviewing and Editing

Yi Liu: Conceptulization; Data curation; Software; Formal analysis; Writing, Reviewing and Editing; Supervision

Jiang Li: Conceptualization

Zheng N. Fang: Conceptualization; Investigation; Methodology; Formal analysis; Writing, Reviewing and Editing; Supervision

Data availability

Data will be made available on request.

Declaration of competing interest

The authors declare that they have no known competing financial interests or personal relationships that could have appeared to influence the work reported in this paper.

Acknowledgments

This research is supported by the National Science Foundation (Project number: 1832065). We would like to thank the six anonymous reviewers for providing insightful comments that help us make significant improvements to the earlier version of this manuscript.

Appendix A. Supplementary data

Supplementary data to this article can be found online at https://doi.org/10.1016/j.scitotenv.2022.161072.

References

Ahmadlou, M., Al-Fugara, A.K., Al-Shabeeb, A.R., Arora, A., Al-Adamat, R., Pham, Q.B., ... Sajedi, H., 2021. Flood susceptibility mapping and assessment using a novel deep learning model combining multilayer perceptron and autoencoder neural networks. J. Flood Risk Manag. 14 (1), e12683.

Bass, B., Juan, A., Gori, A., Fang, Z., Bedient, P., 2017. 2015 Memorial Day flood impacts for changing watershed conditions in Houston. Natur. Hazards Rev. 18 (3), 05016007.

Bates, P.D., De Roo, A.P.J., 2000. A simple raster-based model for flood inundation simulation. J. Hydrol. 236 (1–2), 54–77.

Bedient, P.B., Holder, A., Vieux, B.E., 2002. A radar-based flood alert system (FAS) designed for Houston, Texas. Global Solutions for Urban Drainage, pp. 1–10.

Bedient, P.B., Holder, A., Benavides, J.A., Vieux, B.E., 2003. Radar-based flood warning system applied to Tropical Storm Allison. J. Hydrol. Eng. 8 (6), 308–318.

Brunner, G.W., 2016a. HEC-RAS River Analysis System, 2D Modeling user's Manual Version 5.0. US Army Corps of Engineers, hydrologic engineering center, Davis.

Brunner, G.W., 2016b. HEC-RAS River Analysis System, Hydraulic Reference Manual, Ver. 5.0. Davis, CA, USA: US Army Corps of Engineers, Hydrologic Engineering Center, cpd-69.

Brunner, G.W., 2021. HEC-RAS River Analysis System, 2D Modeling user's Manual Version 6.0. Davis: US Army Corps of Engineers, hydrologic engineering center.

Carisi, F., Domeneghetti, A., Gaeta, M.G., Castellarin, A., 2017. Is anthropogenic land subsidence a possible driver of riverine flood-hazard dynamics? A case study in Ravenna, Italy. Hydrol. Sci. J. 62 (15), 2440–2455.

Catalao, J., Raju, D., Nico, G., 2020. InSAR maps of land subsidence and sea level scenarios to quantify the flood inundation risk in coastal cities: the case of Singapore. Remote Sens. 12 (2), 296.

Chun, B., Hur, M., Won, J., 2021. Impacts of thermal environments on health risk: a case study of Harris County, Texas. Int. J. Environ. Res. Public Health 18 (11), 5531.

Costabile, P., Costanzo, C., Ferraro, D., Macchione, F., Petaccia, G., 2020. Performances of the new HEC-RAS version 5 for 2-D hydrodynamic-based rainfall-runoff simulations at basin scale: comparison with a state-of-the art model. Water 12 (9), 2326.

Dang, T.D., Cochrane, T.A., Arias, M.E., 2018. Future hydrological alterations in the Mekong Delta under the impact of water resources development, land subsidence and sea level rise. J. Hydrol. Reg. Stud. 15, 119–133.

Dixon, T.H., Amelung, F., Ferretti, A., Novali, F., Rocca, F., Dokka, R., ... Whitman, D., 2006. Subsidence and flooding in New Orleans. Nature 441 (7093), 587–588.

El Shinawi, A., Kuriqi, A., Zelenakova, M., Vranayova, Z., Abd-Elaty, I., 2022. Land subsidence and environmental threats in coastal aquifers under sea level rise and over-pumping stress. J. Hydrol. 608, 127607.

Emanuel, K., 2017. Assessing the present and future probability of Hurricane Harvey's rainfall. Proc. Natl. Acad. Sci. 114 (48), 12681–12684.

EM-DAT. Disaster Profiles, 2020. The OFDA/CRED International Disaster Database, Dec 2020. Retrieved from https://public.emdat.be/.

Farooq, M., Shafique, M., Khattak, M.S., 2019. Flood hazard assessment and mapping of River Swat using HEC-RAS 2D model and high-resolution 12-m TanDEM-X DEM (WorldDEM). Natural Hazards 97 (2), 477–492.

FEMA, 2020. FIMA NFIP Redacted Claims Data Set, Dec 2020. Retrieved from https://www.fema.gov/openfema-data-page/fima-nfip-redacted-claims.

Galloway, D.L., Jones, D.R., Ingebritsen, S.E. (Eds.), 1999. Land Subsidence in the United States. vol. 1182. US Geological Survey.

Gao, S., Zhang, J., Li, D., Jiang, H., Fang, Z.N., 2021. Evaluation of multiradar multisensor and stage IV quantitative precipitation estimates during hurricane Harvey. Natur. Hazards Rev. 22 (1), 04020057.

Garcia, M., Juan, A., Bedient, P., 2020. Integrating reservoir operations and flood modeling with HEC-RAS 2D. Water 12 (8), 2259.

Goodell, C., 2014, December 8. Including Channel Bathymetry into your Terrain. The RAS Solution. https://www.kleinschmidtgroup.com/ras-post/including-channel-bathymetry-into-your-terrain/.

Grimaldi, S., Schumann, G.P., Shokri, A., Walker, J.P., Pauwels, V.R.N., 2019. Challenges, opportunities, and pitfalls for global coupled hydrologic-hydraulic modeling of floods. Water Resour. Res. 55 (7), 5277–5300.

Habib, E., Larson, B.F., Graschel, J., 2009. Validation of NEXRAD multisensor precipitation estimates using an experimental dense rain gauge network in south Louisiana. J. Hydrol. 373 (3–4), 463–478.

Hanson, S., Nicholls, R., Ranger, N., Hallegatte, S., Corfee-Morlot, J., Herweijer, C., Chateau, J., 2011. A global ranking of port cities with high exposure to climate extremes. Clim. Chang. 104 (1), 89–111.

HCFCD, Harris County Flood Control District, 2020a. Model and Map Management (M3) System. accessed in 2020. Retrieved from https://www.hcfcd.org/Interactive-Mapping-Tools/MODEL-AND-MAP-MANAGEMENT-M3-SYSTEM.

HCFCD, Harris County Flood Control District, 2020b. Harris County Flood Warning System. accessed in 2020. https://www.harriscountyfws.org/?View=full.

HCFCD, Harris County Flood Control District, 2020c. Historical High Water Marks. accessed in 2020. Available at https://www.arcgis.com/home/item.html?id=bd266d344dab42b993c5d4f0b4599282.

HDSC, Hydrometeorological Design Studies Center, 2017. Hurricane Harvey, 25–31 August 2017 Annul Exceedance Probabilities for the Worst Case 4-day Rainfall. Available at

https://hdsc.nws.noaa.gov/pub/hdsc/data/aep/201708_Harvey/AEP_HurricaneHarvey_August2017.pdf.
Hoffmann, J., Leake, S.A., Galloway, D.L., Wilson, A.M., 2003. MODFLOW-2000 groundwater Model–User Guide to the Subsidence and Aquifer-system Compaction (SUB) Package. Geological Survey Washington DC.
Holzer, T.L., Bluntzer, R.L., 1984. Land subsidence near oil and gas fields, Houston, Texas a. Groundwater 22 (4), 450–459.
Holzer, T.L., Johnson, A.I., 1985. Land subsidence caused by ground water withdrawal in urban areas. GeoJournal 11 (3), 245–255.
Hsu, P.H., Su, W.R., Tsai, C.H., 2010, July. Land subsidence analysis and inundation prediction based on multi-temporal digital elevation model data. 2010 IEEE International Geoscience and Remote Sensing Symposium. IEEE, pp. 3339–3342.
Ito, Y., Chen, H., Sawamukai, M., Su, T., Tokunaga, T., 2015. An analysis on the relationship between land subsidence and floods at the Kujukuri Plain in Chiba Prefecture, Japan. Proceedings of the International Association of Hydrological Sciences. vol. 372, pp. 163–167.
Jonkman, S.N., Godfroy, M., Sebastian, A., Kolen, B., 2018. Brief communication: loss of life due to Hurricane Harvey. Nat. Hazards Earth Syst. Sci. 18 (4), 1073–1078.
Karim, I.R., Hassan, Z.F., Abdullah, H.H., Alwan, I.A., 2021. 2D-HEC-RAS modeling of flood wave propagation in a semi-arid area due to dam overtopping failure. Civil Eng. J. 7 (9), 1501–1514.
Kasmarek, M.C., 2013. Hydrogeology and Simulation of Groundwater Flow and Land-Surface Subsidence in the Northern Part of the Gulf Coast Aquifer System, Texas, 1891–2009, U.S. Geological Survey Scientific Investigations Report 2012–5154.
Kasmarek, M.C., Gabrysch, R.K., Johnson, M.R., 2009. Estimated Land-surface Subsidence in Harris County, Texas, 1915–17 to 2001. US Department of the Interior, US Geological Survey.
Kellens, W., Terpstra, T., De Maeyer, P., 2013. Perception and communication of flood risks: a systematic review of empirical research. Risk Anal. 33 (1), 24–49.
Khan, S.I., Hong, Y., Wang, J., Yilmaz, K.K., Gourley, J.J., Adler, R.F., Irwin, D., 2010. Satellite remote sensing and hydrologic modeling for flood inundation mapping in Lake Victoria basin: implications for hydrologic prediction in ungauged basins. IEEE Trans. Geosci. Remote Sens. 49 (1), 85–95.
Kim, V., Tantanee, S., Suparta, W., 2020. GIS-based flood hazard mapping using HEC-RAS model: a case study of Lower Mekong River, Cambodia. Geogr. Tech. 15 (1).
Legates, D.R., McCabe Jr., G.J., 1999. Evaluating the use of "goodness-of-fit" measures in hydrologic and hydroclimatic model validation. Water Resour. Res. 35 (1), 233–241.
Li, X., Rankin, C., Gangrade, S., Zhao, G., Lander, K., Voisin, N., ... Gao, H., 2021. Evaluating precipitation, streamflow, and inundation forecasting skills during extreme weather events: a case study for an urban watershed. J. Hydrol. 603, 127126.
Lin, Y., Mitchell, K.E., 2005. 1.2 the NCEP stage II/IV hourly precipitation analyses: Development and applications. Proceedings of the 19th Conference Hydrology, American Meteorological Society, San Diego, CA, USA. vol. 10.
Liu, Y., Li, J., Fang, Z.N., 2019. Groundwater level change management on control of land subsidence supported by borehole extensometer compaction measurements in the Houston-Galveston Region, Texas. Geosciences 9 (5), 223.
Liu, Y., Li, J., Fasullo, J., Galloway, D.L., 2020. Land subsidence contributions to relative sea level rise at tide gauge Galveston Pier 21, Texas. Sci. Rep. 10 (1), 1–11.
Mediero, L., Garrote, L., Martín-Carrasco, F.J., 2011. Probabilistic calibration of a distributed hydrological model for flood forecasting. Hydrol. Sci. J. 56 (7), 1129–1149.
Michel-Kerjan, E., Kunreuther, H., 2011. Redesigning flood insurance. Science 333 (6041), 408–409.
Miller, M.M., Shirzaei, M., 2019. Land subsidence in Houston correlated with flooding from hurricane Harvey. Remote Sens. Environ. 225, 368–378.
Miller, R. L., Fram, M., Fujii, R., & Wheeler, G. (2008). Subsidence reversal in a re-established wetland in the Sacramento-San Joaquin Delta, California, USA. San Francisco Estuary and Watershed Science, vol. 6(3).
Munawar, H.S., Hammad, A., Ullah, F., Ali, T.H., 2019, December. After the flood: a novel application of image processing and machine learning for post-flood disaster management. Proceedings of the 2nd International Conference on Sustainable Development in Civil Engineering (ICSDC 2019), Jamshoro, Pakistan, pp. 5–7.
Nelson, B.R., Prat, O.P., Seo, D.J., Habib, E., 2016. Assessment and implications of NCEP Stage IV quantitative precipitation estimates for product intercomparisons. Weather Forecast. 31 (2), 371–394.
NOAA, 2020. Storm Events Database. Available at NOAA site https://www.ncdc.noaa.gov/stormevents/.
Ongdas, N., Akiyanova, F., Karakulov, Y., Muratbayeva, A., Zinabdin, N., 2020. Application of HEC-RAS (2D) for flood hazard maps generation for Yesil (Ishim) river in Kazakhstan. Water 12 (10), 2672.
Ouyang, M., Ito, Y., Tokunaga, T., 2020. Local land subsidence exacerbates inundation hazard to the Kujukuri Plain, Japan. Proceedings of the International Association of Hydrological Sciences 382, 657–661.
Patel, D.P., Ramirez, J.A., Srivastava, P.K., Bray, M., Han, D., 2017. Assessment of flood inundation mapping of Surat city by coupled 1D/2D hydrodynamic modeling: a case application of the new HEC-RAS 5. Nat. Hazards 89 (1), 93–130.
Penning-Rowsell, E., Floyd, P., Ramsbottom, D., Surendran, S., 2005. Estimating injury and loss of life in floods: a deterministic framework. Nat. Hazards 36 (1–2), 43–64.
Rajib, A., Liu, Z., Merwade, V., Tavakoly, A.A., Follum, M.L., 2020. Towards a large-scale locally relevant flood inundation modeling framework using SWAT and LISFLOOD-FP. J. Hydrol. 581, 124406.
Rodolfo, K.S., Siringan, F.P., 2006. Global sea-level rise is recognized, but flooding from anthropogenic land subsidence is ignored around northern Manila Bay, Philippines. Disasters 30 (1), 118–139.
Shareef, M.E., Abdulrazzaq, D.G., 2021. River flood modelling for flooding risk mitigation in Iraq. Civil Eng. J. 7 (10), 1702–1715.
Shirzaei, M., Bürgmann, R., 2018. Global climate change and local land subsidence exacerbate inundation risk to the San Francisco Bay Area. Sci. Adv. 4 (3), eaap9234.
Shrestha, A., Bhattacharjee, L., Baral, S., Thakur, B., Joshi, N., Kalra, A., Gupta, R., 2020, May. Understanding suitability of MIKE 21 and HEC-RAS for 2D floodplain modeling. World Environmental and Water Resources Congress 2020: Hydraulics, Waterways, and Water Distribution Systems Analysis. American Society of Civil Engineers, Reston, VA, pp. 237–253.
Shustikova, I., Domeneghetti, A., Neal, J.C., Bates, P., Castellarin, A., 2019. Comparing 2D capabilities of HEC-RAS and LISFLOOD-FP on complex topography. Hydrol. Sci. J. 64 (14), 1769–1782.
Stork, S.V., Sneed, M., 2002. Houston-Galveston Bay area, Texas, from space—a new tool for mapping land subsidence. US Geol. Survey Fact Sheet 110, 2.
Tayefi, V., Lane, S.N., Hardy, R.J., Yu, D., 2007. A comparison of one-and two-dimensional approaches to modelling flood inundation over complex upland floodplains. Hydrol. Proc. 21 (23), 3190–3202.
Viero, D.P., Roder, G., Matticchio, B., Defina, A., Tarolli, P., 2019. Floods, landscape modifications and population dynamics in anthropogenic coastal lowlands: The Polesine (northern Italy) case study. Sci. Tot. Environ. 651, 1435–1450.
Vieux, B.E., Bedient, P.B., 2004. Assessing urban hydrologic prediction accuracy through event reconstruction. J. Hydrol. 299 (3–4), 217–236.
Walker, K., Shelton, K., 2016. Houston in Flux: Understanding a Decade of Bayou City Development.
Wang, J., Gao, W., Xu, S., Yu, L., 2012. Evaluation of the combined risk of sea level rise, land subsidence, and storm surges on the coastal areas of Shanghai, China. Clim. Chang. 115 (3), 537–558.
Yin, J., Yu, D., Yin, Z., Wang, J., Xu, S., 2013. Modelling the combined impacts of sea-level rise and land subsidence on storm tides induced flooding of the Huangpu River in Shanghai, China. Clim. Chang. 119 (3–4), 919–932.
Yin, J., Yu, D., Wilby, R., 2016. Modelling the impact of land subsidence on urban pluvial flooding: a case study of downtown Shanghai, China. Sci. Total Environ. 544, 744–753.
Yu, D., Lane, S.N., 2011. Interactions between subgrid-scale resolution, feature representation and grid-scale resolution in flood inundation modelling. Hydrol. Process. 25 (1), 36–53.
Yu, J., Wang, G., Kearns, T.J., Yang, L., 2014. Is there deep-seated subsidence in the Houston-Galveston area? Int. J. Geophys. 2014.
Zeiger, S.J., Hubbart, J.A., 2021. Measuring and modeling event-based environmental flows: an assessment of HEC-RAS 2D rain-on-grid simulations. J. Environ. Manag. 285, 112125.
Zhao, Q., Pan, J., Devlin, A., Xu, Q., Tang, M., Li, Z., ... Pepe, A., 2021. Integrated analysis of the combined risk of ground subsidence, sea level rise, and natural hazards in coastal and Delta River Regions. Remote Sens. 13 (17), 3431.